Electric field tuning of ultrafast demagnetization in a magnetoelectric heterostructure

A. R. Will-Cole [1,*] Chuangtang Wang,[1,*] Nirjhar Bhattacharjee,[1] Yongmin Liu,[1,2,†] and N. X. Sun [1,‡]

[1]*Department of Electrical and Computer Engineering, Northeastern University, Boston, Massachusetts 02115, USA*
[2]*Department of Mechanical and Industrial Engineering, Northeastern University, Boston, Massachusetts 02115, USA*

Voltage/electric-field control of ultrafast magnetization dynamics in magnetoelectrics provides a novel avenue for electronic tuning with orders of magnitude less power consumption, improved tuning response time, and more compact form factor, compared with conventional magnetic field control of magnetization dynamics. Magnetoelectrically tuned laser-driven magnetization dynamics has the potential to enable the next generation of optomagnetic devices from THz communication to optical magnetic recording. In this study, we fabricated a magnetoelectric heterostructure, specifically ferromagnetic $(Fe_{81}Ga_{19})_{88}B_{12}$ (FeGaB) thin film deposited on a $Pb(Mg_{1/3}Nb_{2/3})O_3$-$PbTiO_3$ ferroelectric substrate, to explore the electric field tuning of ultrafast demagnetization and to understand how magnetic anisotropy changes postdemagnetization. We characterized the magnetoelectric coupling of our heterostructure to demonstrate the static and dynamic magnetization tunability with an applied electric field. We utilized the time-resolved magneto-optic Kerr effect to understand the ultrafast demagnetization process under different applied electric fields and magnetic fields. The typically observed strain-induced magnetic easy-axis rotation in a ferromagnetic/ferroelectric heterostructure was also observed to tune the ultrafast demagnetization of FeGaB in our experiment. Additionally, we found that the magnetization rotation can be achieved with a lower electric field compared with static tuning without laser heating. Furthermore, we observed the hysteresis loops postultrafast demagnetization and found that the magnetoelectric heterostructure exhibits a mixture of volatile and nonvolatile behaviors. These findings shed light on the potential of our magnetoelectric heterostructure for ultrafast optomagnetic devices and electric field tuning of spintronic THz emitters.

I. INTRODUCTION

Since the discovery of ultrafast quenching of the magnetic order in ferromagnetic Ni thin films on an unprecedented 200–300 femtosecond (fs) time scale and subsequently the measurement of the terahertz (THz)-range emission based on magnetic dipole oscillation by Beaurepaire *et al.*, there has been heightened interest in magnetism in the subpicosecond regime [1,2]. Ultrafast quenching of the magnetic order, also known as laser-driven demagnetization or ultrafast demagnetization [3,4], is a method to rapidly manipulate magnetization with light, for instance, a coherent control of magnetization within 20 fs in an antiferromagnet [5]. This phenomenon is interesting not only from a fundamental perspective but also for applications requiring rapid all-optical switching for magnetic recording or magnetic-dipole-based THz emission from ferromagnetic films [6,7]. More recently, ultrafast demagnetization has garnered attention as a spintronic THz emitter, because of the reported large THz emission from magnetic films with only several nanometers (nm) in thickness [8,9]. The ultrafast demagnetization of the ferromagnet diffuses spin current into an adjacent heavy metal which converts the spin

current to charge current due to the inverse spin Hall effect and results in a radiated THz signal (electric-dipole based THz emission) [9]. The ultrafast demagnetization phenomenon has been extensively studied for transition metal element-based thin films, such as Ni, Co, and Fe. The behavior of these materials is well characterized by the phenomenologically developed three-temperature model and, more recently, the microscopic three-temperature model which is based on the heating of the spin system in a single ferromagnetic layer and accounts for the interplay between lattice, electron, and spin subsystems [1,10,11]. Additionally, ultrafast demagnetization has been investigated in noniterant ferromagnets, and in materials with ferro- or antiferromagnetically coupled sublattices, such as ferrimagnetic materials with two sublattices aligned antiparallel, e.g., rare-earth-based GdFeCo alloys [12–14], and permalloy with Fe and Ni sublattices ferromagnetically coupled [15].

The tuning of the ultrafast demagnetization phenomenon has been studied more recently [16–19]. It has been shown that the demagnetization at the time scale of several hundred fs is stronger at longer pump wavelengths—this is explained by the wavelength dependence of the laser-induced heating of the electrons in the microscopic three-temperature model [16–18]. Beyond the wavelength dependence, the laser fluence, polarization, and pulse duration allow for control over the total absorbed energy into the ferromagnetic film and therefore represent strategies to tune ultrafast

174401-1

demagnetization [19,20]. Additionally, demagnetization processes have been manipulated in a CoFeB-based magnetic tunnel junction via external bias applied to the junction, which is attributed to the changes in the junction conductivity [21]. Further work on CoFeB suggested that crystalline disorder can enhance spin-lattice scattering during ultrafast demagnetization (promoted by single cycle THz fields) [22]. In this study, we have investigated the potential for electric field (E field) tuning of ultrafast demagnetization in a ferromagnet (FM)/ferroelectric (FE) magnetoelectric (ME) heterostructure, specifically $(Fe_{80}Ga_{20})B_{12}$ (FeGaB) thin film deposited directly on a $Pb(Mg_{1/3}Nb_{2/3})O_3$-$PbTiO_3$ (PMN-PT) substrate. This experimental study demonstrates the utilization of the magnetoelectric (ME) heterostructures for ultrafast demagnetization tuning, which may have implications for tunable THz emitters. It should be noted that there have been notable demonstrations of laser excitation on single-phase materials, such as pump excitation of ferroelectric and antiferromagnetic ordering in $GdFeO_3$ [23], and photoinduced magnetoelectricity in CuB_2O_4 [24]. Additionally, ultrafast laser pump excitation has been shown to tune antiferromagnetic phase transitions in CuO [25]. Antiferromagnetic domains in Y-type hexaferrite $(Ba, Sr)_2Me_2Fe_{12}O_{22}$ ($Me =$ divalent transition metal) have been studied utilizing the charge-magnetic interference effect with resonant x-ray dichroism from magnetic scattering [26]. There has been exploration in ME heterostructures, such as the control of ferroelectric order on a time scale dictated by spin-lattice relaxation in the FM material of the ME stack $Ba_{0.1}Sr_{0.9}TiO_3$/$La_{0.7}Ca_{0.3}MnO_3$ [27].

The FeGaB/PMN-PT ME heterostructure was selected for our experimental study. We selected FeGaB as our magnetic film because ferrite/ferroelectric composites have ME coupling coefficients limited to several $Oe\,cm\,kV^{-1}$, while FeGaB/FE-like bilayers have achieved ME coupling coefficients up to 94 $Oe\,cm\,kV^{-1}$ [28,29]. ME coupling is the control of electric polarization switching through an applied magnetic field (direct ME effect) and the control of magnetization through an applied electric field (converse ME effect). While ME effects were first theorized and experimentally demonstrated for a single-phase material, van Suchtelen *et al.* proposed the ME effect for composite materials [30–34]. A key advantage of ME composites over single-phase multiferroics is the expansive material possibilities because ME composites circumvent the contrasting chemical requirements that limit single-phase multiferroics [35]. Additionally, ME composites exhibit significantly higher ME voltage than single-phase multiferroics, like $BiFeO_3$ [36]. ME horizontal, laminar heterostructures have coupling between the magnetic and electrical energy realized through a mechanical interface between the FM/piezoelectric layer. The converse ME effect has been experimentally demonstrated in multiple heterostructures where magnetic films, such as permalloy ($Ni_{80}Fe_{20}$), FeGa alloys (B-doped $Fe_{80}Ga_{20}$), FeCo alloys ($Fe_{50}Co_{50}$), and ferrites (Fe_3O_4 and $CoFe_2O_4$) grown directly on FE substrate, like $Pb(Zn_{1/3}Nb_{2/3})O_3$-$PbTiO_3$(PZN-PT), $Pb(Mg_{1/3}Nb_{2/3})O_3$-PbTiO$_3$ (PMN-PT), and $Pb(In_{1/2}Nb_{1/2})O_3$-$Pb(Mg_{1/3}Nb_{2/3})O_3$-PbTiO$_3$ (PIN-PMN-PT) [29,37–41]. The current state-of-the-art magnetic

materials for ME composites are B- and C-doped FeGa alloys, $(Fe_{81}Ga_{19})_{88}B_{12}$ and $(Fe_{81}Ga_{19})_{88}C_{12}$, and $(Fe_{90}Co_{10})_{78}Si_{12}B_{10}$ [42–46]. Here we use $(Fe_{81}Ga_{19})_{88}B_{12}$ (FeGaB) in our ME heterostructure, because FeGaB has a high magnetomechanical coupling factor of 0.84, compared to $(Fe_{90}Co_{10})_{78}Si_{12}B_{10}$ (0.67) and Terfenol-D (0.18); magnetomechanical coupling of unity (1) represents complete transduction between magnetic and elastic energy [45,47,48]. Additionally, FeGaB has a high saturation magnetostriction of 70 ppm and narrow ferromagnetic resonance linewidth of 20 Oe [42,44,45]. Thus, FeGaB is an excellent state-of-the-art magnetic material for our ME heterostructure. For our FE substrate, we have selected PMN-PT because it is a relaxor-based FE crystal with composition near the morphotropic phase boundary and therefore has a high dielectric constant and ultrahigh piezoelectricity [49]. Specifically, we employ (011)-cut PMN-PT because when poled this crystal exhibits anisotropic in-plane piezoelectric coefficients ($d_{31} \sim -1750\,pC/N$ and $d_{32} \sim 900\,pC/N$) capable of generating giant in-plane, uniaxial magnetic anisotropy field in the magnetic film [37,50].

Our foundational approach for demonstrating FeGaB/PMN-PT heterostructure for ultrafast control of magnetism is substantiated via multiple experimental strategies. After fabrication of the FeGaB/PMN-PT heterostructure the ME heterostructure was characterized for material quality. This was first accomplished by ensuring that the applied E-field induced strain in the PMN-PT substrate followed by experimental validation of the ME coupling, e.g., static, and dynamic magnetization control with applied E field. Next, to show the feasibility of this ME heterostructure and its potential for use in applications requiring the magnetization rotation, such as voltage tunable THz emitters, we demonstrated E-field tuning of ultrafast demagnetization using time-resolved magneto-optic Kerr effect (TR-MOKE) spectroscopy. Last, we investigated how ultrafast demagnetization can alter the magnetic anisotropy of the ME heterostructure and lower the required E field for magnetization rotation compared to the equilibrium case. The details of each experimental strategy are explained and discussed herein.

II. RESULTS AND DISCUSSION

The ME heterostructure of 50-nm FeGaB on (011)-cut PMN-PT substrate was fabricated by sputter deposition. Before the deposition of the FeGaB film on the substrate, top and bottom Cu electrodes (8 and 50 nm respectively) were deposited on the (011)-cut PMN-PT single crystal (0.5 mm thick) and the crystal was prepoled along the thickness direction at 200 °C (temperature above the Curie temperature of 150 °C) in an oil bath. Prepoling of the PMN-PT is necessary to align the ferroelectric domains, such that there are no nonuniform residual stresses applied to the magnetic film after deposition. The FeGaB was fabricated with base pressures lower than 1×10^{-7} Torr to reduce contamination and under an *in situ* magnetic field to induce a uniaxial, in-plane magnetic anisotropy—see easy and hard axis magnetization hysteresis loop results in measured with a LakeShore
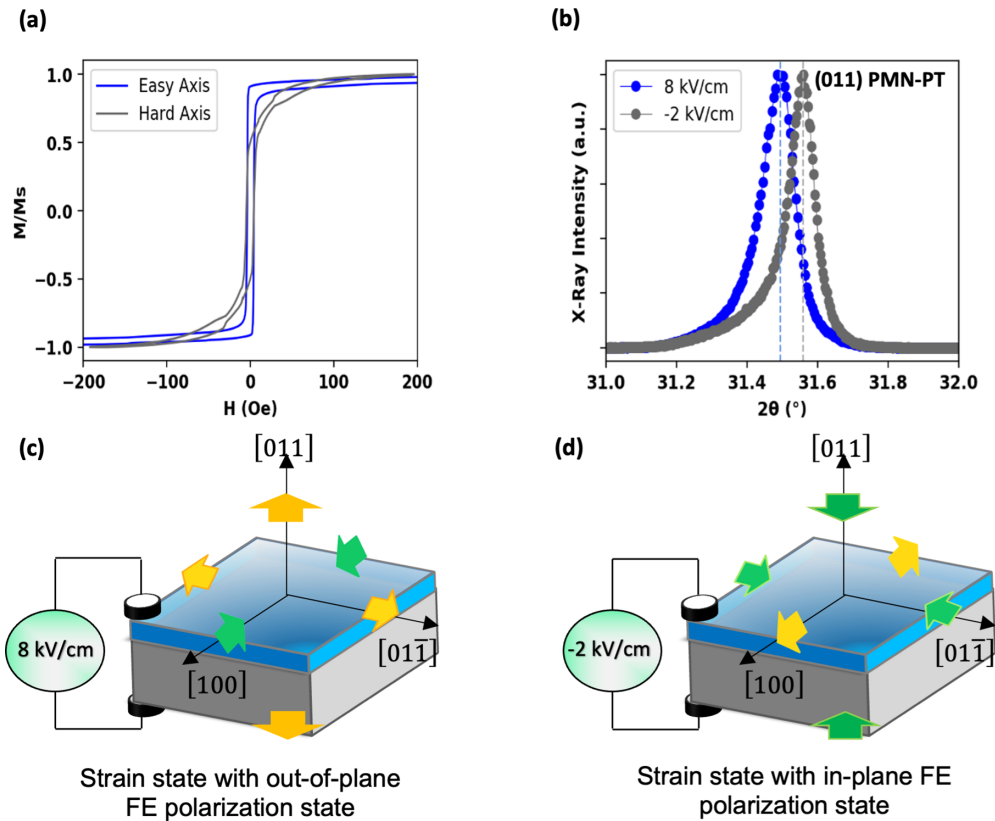
FIG. 1. (a) Vibrating sample magnetometry of the easy-axis (along the [100] of PMN-PT) and hard-axis (along the [01-1] of PMN-PT) directions produced due to deposition under DC magnetic bias. (b) X-ray diffraction pattern about the (011) PMN-PT substrate diffraction peak with applied E field -2 kV/cm (grey) and 8 kV/cm (blue). There is a shift to $0.064\,^{\circ}$ in the PMN-PT (011) substrate peak to a lower two-theta position. (c) Schematic of the PMN-PT strain state with out-of-plane polarization. (d) Schematic of the PMN-PT strain state with predominately in-plane polarization. Gold arrows represent tensile strain and green arrows represent compressive strain in schematics (c) and (d).

7407 vibrating sample magnetometer (VSM). A 2-nm-thick Cu seed layer was deposited before the magnetic film to promote magnetic softness (underlayer effect) [51,52] and a 2-nm-thick Cu capping layer to prevent oxidation of the magnetic film. Ag/In contacts were implemented to create an electrical contact to the top and bottom surface of the ME heterostructure via Cu wire. The E field is applied along the surface normal direction (through thickness) of the heterostructure.

To substantiate the quality of the ME heterostructure, e.g., to ensure that the applied E field results in strain of the PMN-PT substrate, we performed high angle, out-of-plane x-ray diffraction (XRD) as a function of E-field materials characterization experiments at room temperature. The XRD was performed with a four-circle diffractometer Rigaku SmartLab (Cu $K\alpha$ radiation), and the spectra were obtained from symmetric $2\theta - \omega$ scans. The XRD spectra with applied E field are shown in Fig. 1(b). Comparing $+8$ kV/cm applied along the [011] direction with -2 kV/cm applied along the [011] direction, we see a $0.064\,^{\circ}$ shift in the PMN-PT (011) substrate peak to a lower two-theta position, which corresponds to an increase in d spacing out-of-plane and indicates tensile strain in the $+8$-kV/cm case. This is evidence of the two strain states in the (011)-cut PMN-PT enabled with applied E field—(1) polarization aligned out of plane [Fig. 1(c)], and (2) majority

of the ferroelectric domains lying in plane [Fig. 1(d)]. The polarization rotation is accompanied by large in-plane and out-of-plane strain in the single crystal PMN-PT [53].

Additional quantification of the ME heterostructure materials quality was attained by verifying the ME coupling via static and dynamic magnetic characterization methods, namely VSM and ferromagnetic resonance (FMR) with applied E field at room temperature. The magnetization hysteresis loops were measured along the [100] in-plane direction of the PMN-PT with applied E field ranging from -2 to $+8$ kV/cm as seen in . As evident by Fig. 2(a), there are large, E-field induced effective magnetic anisotropy changes as we anticipated based on previous literature—sweeping from -2 to $+8$ kV/cm corresponds to an increase in the magnetic anisotropy field [29,37]. The degree of the E-field tuning is obvious by the tuning of the magnetic hysteresis loop squareness, remnant magnetization normalized to the saturation magnetization or the M_R/M_S, as shown in Table I. We observe 56% tunability in the squareness (M_R/M_S) of the magnetic hysteresis loop, which is a measure of the static magnetization control. We also performed broadband strip line FMR measurements to understand the E-field tuning of the dynamic property of the ME heterostructure. As shown in Fig. 2(b), we performed the DC magnetic field sweep ferromagnetic resonance at a frequency of 8 GHz and measured
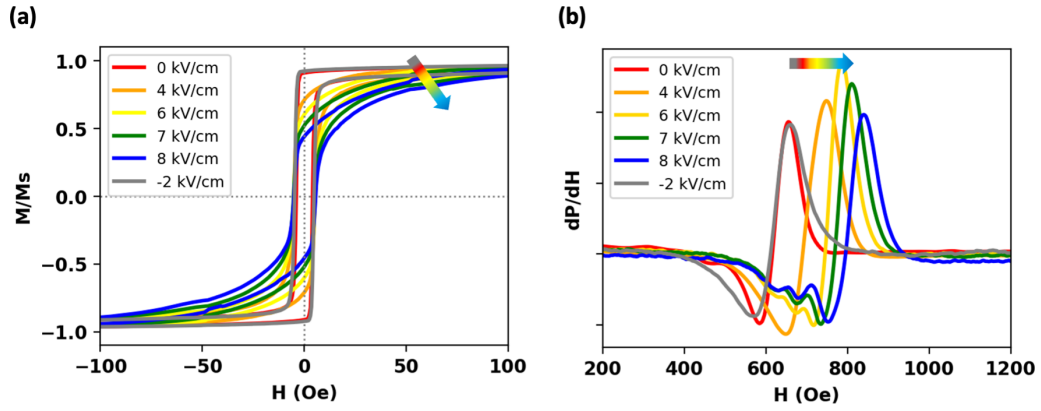
FIG. 2. (a) Magnetic hysteresis loops measured with applied E field ranging from -2 to 8 kV/cm. This measurement was collected with the DC magnetic field applied parallel to the [100] direction of the PMN-PT crystal. The magnetization is normalized to saturation magnetization. The arrow represents increasing applied E field. (b) Magnetic field sweep ferromagnetic resonance at 8 GHz with applied E field ranging from -2 to 8 kV/cm. This measurement was collected with the DC magnetic field applied parallel to the [100] in-plane direction of the PMN-PT crystal. First-order standing spin wave modes along the film thickness direction emerge for higher applied E field at DC magnetic fields lower than the main resonance mode. The arrow represents increasing applied E field.

along the [100] in-plane direction of the PMN-PT. There is an increase in the resonance field (H_{RES}) with increase in applied E field—this shift in the resonance field tuning is explicitly shown in Table I. We see an approximate 200-Oe shift in the FMR field from -2 to $+8$ kV/cm. This E-field tuning of the resonance field can be explained by the strain-mediated in-plane magnetic anisotropy term H_{EFF}. The resonance field is tuned to higher or lower field values depending on whether H_{EFF} is parallel or perpendicular to the applied DC magnetic field, and the amplitude of the shift in resonance field is proportional to the applied E field. For in-plane FMR this is described by the Kittel equation as follows [54]:

$$f = \gamma \sqrt{(H_{RES} + H_K + H_{EFF})(H_{RES} + H_K + H_{EFF} + 4\pi M_S)}.$$
$$(1)$$

In Eq. (1) γ is the gyromagnetic ratio (2.8 MHz/Oe), H_K is defined as the in-plane anisotropy field, and M_S is the saturation magnetization. H_{EFF} is the effective magnetic field produced due to the piezoelectric strain in the PMN-PT and induced in-plane stress in the FeGaB film and ΔH_{EFF} defined by Eq. (2) [29],

$$\Delta H_{EFF} = 3\lambda_S d_{EFF} E Y / M_S$$
$$(2)$$

In Eq. (2) λ_S is the saturation magnetostriction and Y is the Young's modulus of the FeGaB. E is defined as the applied E

field. Equation (2) is valid in the regime where the thickness of the FeGaB film and Cu electrodes are much less than the PMN-PT substrate, such that the FeGaB is coherently strained in plane due to the piezoelectric strain in the PMN-PT single crystal. The effective piezoelectric coefficient d_{EFF} is given by Eq. (3) [29],

$$d_{EFF} = (d_{31} - d_{32})/1 + \nu.$$
$$(3)$$

In Eq. (3) ν is the Poisson ratio of the FeGaB, and the anisotropic piezoelectric coefficients of the PMN-PT are defined by the d_{31} and d_{32}. Equation (3) is derived assuming a plane stress condition. Theoretical calculation of the magnetic anisotropy field using (2) and (3) in the FeGaB film estimates approximately 250 Oe with $+8$ kV/cm applied, which is comparable to the 200 Oe experimentally determined in Fig. 2(b). This discrepancy may arise from variation in the FeGaB saturation magnetostriction value as it varies with minor changes in stoichiometry or a variation in the piezoelectric coefficients of the PMN-PT substrate as slight composition variations at the morphotropic phase boundary can correspond to significant changes in piezoelectric properties [55]. It is important to note that photoinduced strain can also tune the ferromagnetic resonance field as demonstrated on Bi-doped yttrium-iron-garnet films [56], however here we focus on strain produced by the PMN-PT substrate. In our experiments, the E-field tunability observed in the static and dynamic magnetic characterization confirms the presence of converse ME coupling (shown in Table I).

Subsequent to validating the E-field control of magnetization in our ME heterostructure, we investigated the E-field tuning of ultrafast demagnetization with time-resolved magneto-optic Kerr effect spectroscopy. An 80-MHz mode-locked Ti-sapphire laser with a pulse duration of 200 fs and a center wavelength of 800 nm was employed in our experiment. Eighty percent of the 800-nm beam passed through a BBO crystal to generate 400-nm pulses through the second harmonic generation and were modulated to the frequency of 10 MHz via an electro-optical modulator. The remaining 20% of the 800-nm beam was used as the probe beam and

TABLE I. E-field tuning of $(Fe_{80}Ga_{20})_{88}B_{12}$/PMN-PT heterostructure*.

	-2 kV/cm	0 kV/cm	4 kV/cm	6 kV/cm	7 kV/cm	8 kV/cm
M_R/M_S	0.891	0.874	0.700	0.602	0.523	0.500
H_{RES}	634 Oe	636 Oe	722 Oe	771 Oe	795 Oe	823 Oe

*Table legend:

M_R is the remnant magnetization.

M_S is the saturation magnetization.

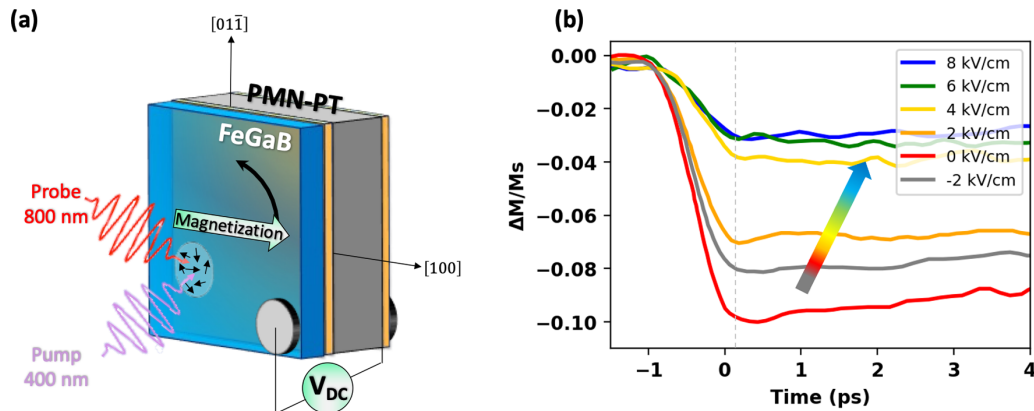H_{RES} is the ferromagnetic resonance field.

FIG. 3. (a) Schematic of ultrafast demagnetization experiment with applied E field. (b) Ultrafast demagnetization curves measured with TR-MOKE along the [100] direction of the PMN-PT with applied E field. The arrow indicates increasing applied E field.

modulated at 200 Hz frequency with an optical chopper. An optical filter was used in front of a balanced photodetector to block the pump light. The 10-MHz high-frequency modulation can suppress the laser intensity noise. However, there was a coherent addition of 10-MHz frequency signals from the function generator and the electro-optical modulator driver. A second 200-Hz low-frequency modulation was used to remove this background signal. The double modulation technique can improve the signal-to-noise ratio of the pump-probe experiment [57]. The pump and probe beams are linearly polarized and both beams were focused on samples with a $20\times$ objective lens. Our measurements were conducted at room temperature. Figure 3(a) illustrates the remnant magnetization dynamics in the FeGaB along the [100] in-plane direction of the PMN-PT single crystal subjected to the applied E field in a longitudinal MOKE geometry with an incident angle of $45°$, and the normalized results are shown in Fig. 3(b). Upon the excitation of the laser pulse, the magnetization of the FeGaB quenches in the first several 100s fs and then recovers at a longer time scale. As the E field decreases from $+8$ to 0 kV/cm (no applied E field), the amplitude of the demagnetization measured along the [100] direction relative to the PMN-PT crystal increases. This behavior is the result of the induced uniaxial anisotropy change due to applied E field. When applying a positive E field, there will be tensile strain transferred to the FeGaB which induces uniaxial anisotropy along the [01-1] direction relative to the PMN-PT. The decrease in the magnitude of the applied, positive E field reduces this induced uniaxial anisotropy and thus the magnetic easy axis as well as the magnetization rotation rotates back to [100] relative to the PMN-PT, therefore enhancing the remnant ultrafast demagnetization. Application of a negative E field should further rotate the easy axis away from the [100] direction relative to the PMN-PT which should result in a reduction in ultrafast demagnetization. This convincingly demonstrates E-field tuning in ME heterostructures, promising ultrafast laser applications that require a magnetization rotation, such as reversible polarization tuning of THz emission. As an example, inverse spin Hall effect emitters produce a linearly polarized E-field pulse that is orthogonal to the FM film magnetization, therefore the in-plane rotation control of the magnetization enables polarization tuning of the

THz signal. It has been very recently demonstrated in inverse spin Hall effect heterostructures, $W/FeCo/TbCo_2/FeCo/Pt$, Pt/NiFe, Pt/CoFeB, Pt/CoFe on PMN-PT substrate [58–60]. We believe that FeGaB/Cu/PMN-PT is a strong candidate for such inverse spin Hall effect THz emission applications if capped with a material with strong spin-orbit coupling and large spin Hall angle, like a heavy metal or three-dimensional (3D) topological insulator [61–66].

Ultrafast laser excitation drives the magnetization into a complicated, higher temperature, nonequilibrium state during the ultrafast demagnetization process, therefore our final experiment was designed to investigate how ultrafast demagnetization process can in turn alter the magnetic anisotropy of our ME heterostructure. This was accomplished by studying the ultrafast demagnetization hysteresis at a postpump demagnetization [the time the postpump was fixed in the experiment as shown by the dashed line in Fig. 3(b)] for the [100] and [01$\bar{1}$] in-plane directions relative to the PMN-PT crystal. The sample was rotated to maintain the longitudinal MOKE geometry. This was repeated under various E-field conditions and the results are summarized in Fig. 4. For the [100] in-plane direction relative to the PMN-PT crystal, we observe a very square hysteresis loop upon the swept magnetic field at 0 kV/cm in Fig. 4(a). The E-field modulation of the nonequilibrium ultrafast demagnetization hysteresis loops with applied E field is directly compared to the equilibrium magnetization hysteresis loops shown in the Supplemental Figs. S1(a) and S1(b) [67]. When applying E field (from $+2$ to $+8$ kV/cm) we observe very hard magnetization loops. For the [01$\bar{1}$] in-plane direction relative to the PMN-PT crystal, we do observe a hard hysteresis loop upon swept magnetic field at 0 kV/cm as shown in Fig. 4(b). However, with increasing the applied E field (from $+2$ to $+8$ kV/cm) we observe squarer magnetization loops. We considered three magnetic anisotropies in our interpretation of the data: (1) the magnetic field induced magnetic anisotropy because of the *in situ* magnetic bias during the deposition along the [100] in-plane direction relative to the PMN-PT crystal, (2) Zeeman energy term due to the presence of the applied DC magnetic field, and, additionally, (3) the magnetoelastic anisotropy from the ME coupling between the FeGaB and PMN-PT. Here we do not include any magnetocrystalline anisotropy, because the FeGaB is
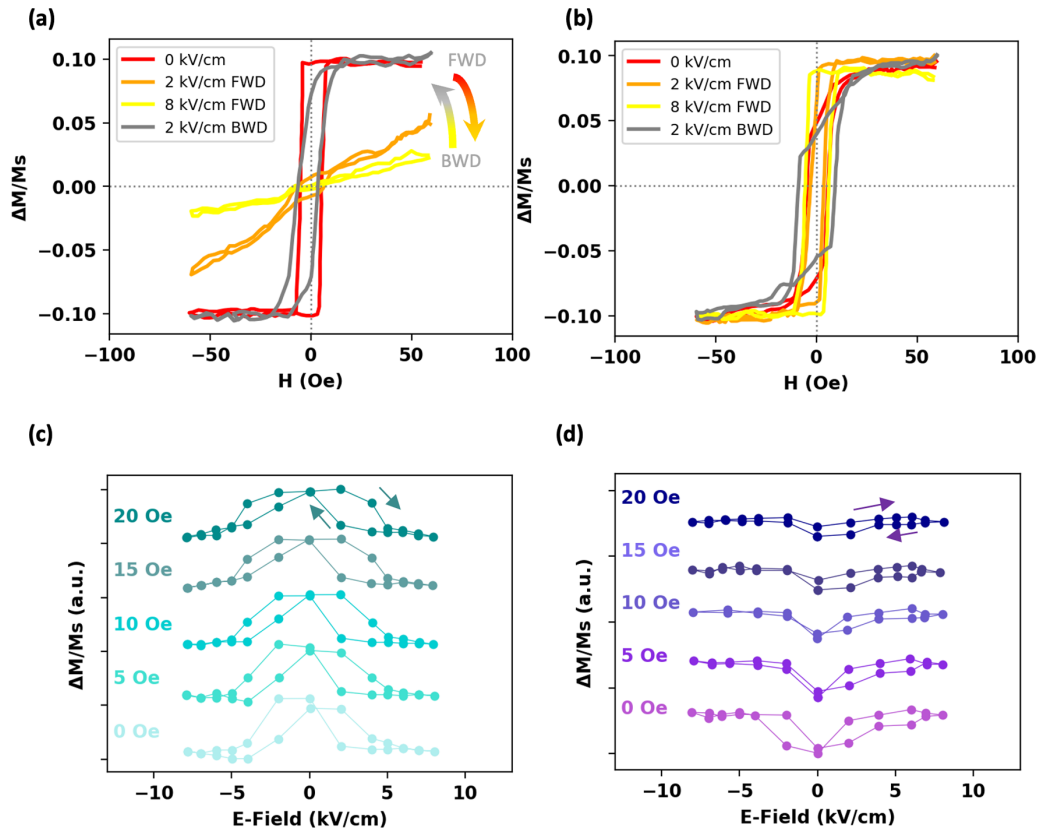
FIG. 4. (a) Normalized magnetization hysteresis loop measured via MOKE after demagnetization as a function of E field. These are measured along the [100] direction relative to the PMN-PT crystal substrate. (b) Normalized magnetization hysteresis loop measured via MOKE after demagnetization as a function of E field. These are measured along the [01-1] direction relative to the PMN-PT crystal substrate. (c) Butterfly loops of the normalized magnetization at the given field value (0, 5, 10, 15, and 20 Oe) after demagnetization at each E-field value measured along the [100] direction relative to the PMN-PT crystal substrate. The results are provided in arbitrary units. (d) Butterfly loops of the normalized magnetization at the given field value (0, 5, 10, 15, and 20 Oe) after demagnetization at each E-field value measured along the [01-1] direction relative to the PMN-PT crystal substrate. The results are provided in arbitrary units.

amorphous. It is important to note that the temperature dependence of the magnetoelastic anisotropy follows the third power law outlined in Eq. (4), where T is temperature, M_S is saturation magnetization, and K is the anisotropy constant,

$$\frac{K(T)}{K(0)} = \left[\frac{M_S(T)}{M_S(0)}\right]^3. \tag{4}$$

This decreases more sharply with increasing temperature than the magnetization and Zeeman energy ($M_S H$, where H is the applied magnetic field and M_S is the saturation magnetization) [68]. From our aforementioned measurements in Figs. 1(a) and 2(a), we can see that the magnetic field induced anisotropy field and magnetoelastic anisotropy field are close to 100 Oe, which is larger than the applied magnetic field in our current measurements, therefore the applied magnetic field plays a secondary role. The magnetic field induced anisotropy is related to the mesoscale structure, for example icosahedral-like clusters give the amorphous CoFeB a magnetic field induced magnetic anisotropy [69]. Additionally, the thermal dependence of magnetization clusters is stronger than for that of a bulk material [70,71]. Therefore, we deduce in our system that the magnetic field induced magnetic anisotropy decreases faster after thermal excitation of the laser compared

with the magnetoelastic anisotropy. In the nonequilibrium state induced by ultrafast demagnetization, the magnetoelastic anisotropy is dominant, therefore the E-field tuning is more effective in the nonequilibrium state compared with the equilibrium state [see Figs. S1(a) and S1(b) in the Supplemental Material [67] for a direct comparison]. This highlights the need to consider the magnetic anisotropy energy changes post-ultrafast demagnetization when designing ME-based devices for magnetization control on a fs time scale [3]. Based on the ratio of the MOKE signal along the easy and hard axis in Figs. 4(a) and 4(b), we can estimate the magnetization rotation. Our ME heterostructure has a magnetization rotation of 59° with a voltage change of 100 V without applied magnetic field, which is at least an eight times enhancement compared to a reported similar structure of Pt/CoFeB with only a 28° magnetization rotation with an applied voltage of 400 V [59]. We have extracted the ultrafast demagnetization intensity at different magnetic fields (0, 5, 10, 15, and 20 Oe) along the [100] and [01$\bar{1}$] directions relative to PMN-PT and plotted these as a function of the applied E field. The results are displayed in Figs. 4(c) and 4(d), respectively. We observe that the ultrafast demagnetization loops along the [100] and [01$\bar{1}$] directions are inverted compared with one another, and this inversion further confirms the rotation of

the magnetic axis with the applied E field [58]. We also observe the piezo-strain butterflylike curve behavior in Fig. 4(c); however, the negative field loop has a reduced area compared with the positive field loop, which indicates asymmetric looplike behavior. Figure 4(d) clearly shows that the loops are a mix of both volatile piezo-strain butterfly looplike curve and nonvolatile strain looplike curve [72,73]. To understand the difference in the nonequilibrium loops to equilibrium loops we direct the reader to Refs. [3,71–74] for results on similar and identical ME heterostructures [74–78]. Overall, we have enhanced control over the magnetization state of this ultrafast demagnetization ME system. The greatest tunability of the magnetization is achieved with a moderate magnetic field applied, because the field is large enough to align the magnetic domains, but weak enough that the strain-induced uniaxial magnetic anisotropy still dominates. We observe less tunability with a relatively small magnetic applied because the field is too weak to align the overall domain structure. Alternatively, a relatively large magnetic field applied will align the magnetic domains but reduce the effect of the strain-induced anisotropy, thus there is a reduced tunability compared with a moderate applied magnetic field.

III. CONCLUSIONS

In summary, we have demonstrated magnetization control in our ME heterostructure composed of PMN-PT/FeGaB and the E-field tuning of ultrafast demagnetization in said heterostructure. We have shown with TR-MOKE that the amplitude of the ultrafast demagnetization curves changes as a function of E field supporting that the magnetization rotates in-plane with applied E field. This effect indicates the promise of ME heterostructures for ultrafast applications requiring magnetic easy-axis rotation control, such as polarization tunable THz emitters based on inverse spin Hall effect or ferromagnetic film based ultrafast demagnetization THz emitters [2,58–60,79,80]. We have also demonstrated how the laser heating effect during ultrafast demagnetization contributes to the changes in magnetic anisotropy compared to equilibrium tuning in a uniformly magnetized film. We attribute these changes to the sharper decrease of the magnetic field induced magnetic anisotropy than the magnetoelastic anisotropy, which allows for the stress anisotropy term derived from ME coupling to dominate. Additionally, the ultrafast demagnetization hysteresis loops showed evidence of both butterflylike volatile and looplike nonvolatile effects for our ME heterostructure. We believe our findings on the E-field control in ME heterostructure would lead to novel applications based on E-field tuning of ultrafast demagnetization-related applications, such as optical magnetization switching relevant for memory/logic devices [81].

[1] E. Beaurepaire, J.-C. Merle, A. Daunois, and J.-Y. Bigot, Phys. Rev. Lett. **76**, 4250 (1996).

[2] E. Beaurepaire, G. M. Turner, S. M. Harrel, M. C. Beard, J.-Y. Bigot, and C. A. Schmuttenmaer, Appl. Phys. Lett. **84**, 3465 (2004).

[3] A. Kirilyuk, A. V. Kimel, and Th. Rasing, Rev. Mod. Phys. **82**, 2731 (2010).

[4] C. Wang and Y. Liu, Nano Convergence **7**, 35 (2020).

[5] D. Bossini, S. Dal Conte, Y. Hashimoto, R. V. Pisarec, Th. Rasing, G. Cerullo, and A. V. Kimel, Nat. Commun. **7**, 10645 (2016).

[6] C. D. Stanciu, F. Hansteen, A. V. Kimel, A. Kirilyuk, A. Tsukamoto, A. Itoh, and T. Rasing, Phys. Rev. Lett. **99**, 047601 (2007).

[7] L. Huang, J.-W. Kim, S.-H. Lee, S.-D. Kim, V. M. Tien, K. P. Shinde, J.-H. Shim, Y. Shin, H. J. Shin, S. Kim *et al.*, Appl. Phys. Lett. **115**, 142404 (2019).

[8] Z. Feng, H. Qiu, D. Wang, C. Zhang, S. Sun, B. Jin, and W. Tan, J. Appl. Phys. **129**, 010901 (2021).

[9] T. Seifer, S. Jaiswal, U. Martens, J. Hannegan, L. Braun, P. Maldonado, F. Freimuth, A. Kronenberg, J. Henrizi, I. Radu, E. Beaurepaire, Y. Mokrousov, P. M. Oppeneer, M. Jourdan, G. Jakob, D. Turchinovich, L. M. Hayden, M. Wolf, M. Münzenberg, M. Kläui, and T. Kampfrath, Nat. Photon. **10**, 483 (2016).

[10] B. Koopmans, *Handbook of Magnetism and Advanced Magnetic Materials* (Wiley, New York, 2007), Vol. 3, pp. 1589–1613.

[11] B. Koopmans, J. J. M. Ruigrok, F. Dalla Longa, and W. J. M. de Jonge, Phys. Rev. Lett. **95**, 267207 (2005).

[12] B. Koopmans, G. Malinoski, F. Dalla Longa, D. Steiauf, M. Fähnle, T. Roth, and M. Aeschlimann, Nat. Mater. **9**, 259 (2010).

[13] C. D. Stanciu, A. Tsukamoto, A. V. Kimel, F. Hansteen, A. Kirilyuk, A. Itoh, and T. Rasing, Phys. Rev. Lett. **99**, 217204 (2007).

[14] R. Medapalli, I. Razdolski, M. Savoini, A. R. Khorsand, A. Kirilyuk, A. V. Kimel, Th. Rasing, A. M. Kalashnikova, A. Tsukamoto, and A. Itoh, Phys. Rev. B **86**, 054442 (2012).

[15] A. J. Schellekens and B. Koopmans, Phys. Rev. B **87**, 020407(R) (2013).

[16] X. Liu, Z. Xu, R. Gao, H. Hu, Z. Chen, Z. Wang, J. Du, S. Zhou, and T. Lai, Appl. Phys. Lett. **92**, 232501 (2008).

[17] G. P. Zhang and W. Hübner, Phys. Rev. Lett. **85**, 3025 (2000).

[18] V. Cardin, T. Balciunas, K. Légaré, A. Baltuska, H. Ibrahim, E. Jal, B. Vodungbo, N. Jaouen, C. Varin, J. Lüning, and F. Légaré, Phys. Rev. B **101**, 054430 (2020).

[19] W. Töws and G. M. Pastor, Phys. Rev. B **100**, 024402 (2019).

[20] B. Vodungbo, J. Gautier, G. Lambert, A. B. Sardinha, M. Lozano, S. Sebban, M. Ducousso, W. Boutu, K. Li, B. Tudu *et al.*, Nat. Commun. **3**, 999 (2012).

[21] M. Savoini, C. Piovera, C. Rinaldi, E. Albisetti, D. Petti, A. R. Khorsand, L. Duò, C. Dallera, M. Cantoni, R. Bertacco, M. Finazzi, E. Carpene, A. V. Kimel, A. Kirilyuk, and T. Rasing, Phys. Rev. B **89**, 140402(R) (2014).

[22] S. Bonetti, M. C. Hoffmann, M.-J. Sher, Z. Chen, S.-H. Yang, M. G. Samant, S. S. P. Parkin, and H. A. Dürr, Phys. Rev. Lett. **117**, 087205 (2016).

[23] Y. M. Sheu, N. Ogawa, Y. Tokunaga, H. C. Chan, and Y. Tokura, Phys. Rev. B **98**, 100301(R) (2018).

[24] D. Bossini, K. Konishi, S. Toyoda, T. Arima, J. Yumoto, and M. Kuwata-Gonokami, Nat. Phys. **14**, 370 (2018).

[25] S. L. Johnson, R. A. de Souza, U. Staub, P. Beaud, E. Möhr-Vorobeva, G. Ingold, A. Caviezel, V. Scagnoli, W. F. Schlotter, J. J. Turner *et al.*, Phys. Rev. Lett. **108**, 037203 (2012).

[26] H. Ueda, Y. Tanaka, Y. Wakabayashi, and T. Kimura, Phys. Rev. B **98**, 134415 (2018).

[27] Y. M. Sheu, S. A. Trugman, L. Yan, Q. X. Jia, A. J. Taylor, and R. P. Prasankumar, Nat. Commun. **5**, 5832 (2014).

[28] A. S. Tatarenko, A. B. Ustinov, G. Srinivasan, V. M. Petrov, and M. I. Bichurin, J. Appl. Phys. **108**, 063923 (2010).

[29] J. Lou, M. Liu, D. Reed, Y. Ren, and N. X. Sun, Adv. Mater. **21**, 4711 (2009).

[30] P. Curie, *J. de Physique. 3e serie*, t.III (1894); reprinted in "Oeuvres de Pierre Curie" (Gauthier-Villars, Paris, 1908), pp. 136, 137.

[31] L. D. Landau and E. M. Lifshitz, *Electrodynamics of Continuous Media* (Addison-Wesley, Reading, MA, 1960).

[32] I. E. Dzyaloshinskii, Zh. Exp. Teor. Fiz. **33**, 881 (1959).

[33] D. N. Astrov, Sov. Phys. JETP **13**, 4 (1961).

[34] J. van Suchtelen, Philips Res. Rep. **27**, 28 (1972).

[35] N. X. Sun and G. Srinivasan, Spin **2**, 124004 (2012).

[36] R. Ramesh and N. A. Spaldin, Nanosci. Technol. **3**, 20 (2009).

[37] J. Lou, D. Reed, C. Pettiford, M. Liu, P. Han, S. Dong, and N. X. Sun, Appl. Phys. Lett. **92**, 262502 (2008).

[38] J. J. Yang, Y. G. Zhao, H. F. Tian, L. B. Lou, H. Y. Zhang, Y. J. He, and H. S. Lou, Appl. Phys. Lett. **94**, 212504 (2009).

[39] M. Liu, O. Obi, Z. Cai, J. Lou, G. Yang, K. S. Ziemer, and N. X. Sun, J. Appl. Phys. **107**, 073916 (2010).

[40] T. Nan, Z. Zhou, M. Liu, X. Yang, Y. Gao, B. A. Assaf, H. Lin, S. Velu, X. Wang, H. Luo *et al.*, Sci. Rep. **4**, 3688 (2014).

[41] M. Staruch, D. B. Gopman, Y. L. Iunin, R. D. Schull, S. F. Cheng, K. Bussmann, and P. Finkel, Sci. Rep. **6**, 37429 (2016).

[42] J. Lou, R. E. Insignares, Z. Cai, K. S. Ziemer, M. Liu, and N. X. Sun, Appl. Phys. Lett. **91**, 182504 (2007).

[43] X. Liang, A. Matyushov, P. Hayes, V. Schell, C. Dong, H. Chen, Y. He, A. Will-Cole, E. Quandt, P. Martins *et al.*, IEEE Trans. Magn. **57**, 8 (2021).

[44] A. R. Will-Cole, A. Gilad Kusne, P. Tonner, C. Dong, X. Liang, H. Chen, and N. X. Sun, IEEE Trans. Magn. **58**, 2800108 (2022).

[45] C. Dong, M. Li, X. Liang, H. Chen, H. Zhou, X. Wang, Y. Gao, M. E. McConney, J. G. Jones, G. J. Brown, B. M. Howe, and N. X. Sun, Appl. Phys. Lett. **113**, 262401 (2018).

[46] V. Hrkac, E. Lage, G. Koppel, J. Strobel, J. McCord, E. Quandt, D. Meyners, and L. Kienle, J. Appl. Phys. **116**, 134302 (2014).

[47] R. Kellogg and A. Flatau, J. Intell. Mater. Syst. Struct. **19**, 5 (2008).

[48] X. H. Song, J. J. Liu, S. H. Wei, X. Y. Zhu, F. Li, Z. R. Zhang, P. Z. Si, and W. J. Ren, Appl. Phys. A **122**, 564 (2016).

[49] S.-E. Park and T. R. Shrout, J. Appl. Phys. **82**, 1804 (1997).

[50] P. Han, W. Yan, J. Tian, X. Huang, and H. Pan, Appl. Phys. Lett. **86**, 052902 (2005).

[51] A. Acosta, K. Fitzell, J. D. Schneider, C. Dong, Z. Yao, R. Sheil, Y. E. Wang, G. P. Carman, N. X. Sun, and J. P. Chang, J. Appl. Phys. **128**, 013903 (2020).

[52] S. Ladak, L. E. Fernández-Outón, and K. O'Grady, J. Appl. Phys. **103**, 07B514 (2008).

[53] J. Heidler, C. Piamonteze, R. V. Chopdekar, M. A. Uribe-Laverde, A. Alberca, M. Buzzi, A. Uldry, B. Delley, C. Bernhard, and F. Nolting, Phys. Rev. B **91**, 024406 (2015).

[54] C. Kittel, J. Phys. Radium **12**, 3 (1951).

[55] F. Li, S. Zhang, D. Lin, J. Luo, Z. Xu, X. Wei, and T. R. Shrout, J. Appl. Phys. **109**, 014108 (2011).

[56] L. Soumah, D. Bossini, A. Anane, and S. Bonetti, Phys. Rev. Lett. **127**, 077203 (2021).

[57] M. J. Gomez, K. Liu, J. G. Lee, and R. B. Wilson, Rev. Sci. Instrum. **91**, 023905 (2020).

[58] A. Chaurasiya, Z. Li, R. Medwal, S. Gupta, J. R. Mohan, Y. Fukuma, H. Asada, E. E. M. Chia, and R. S. Rawat, arXiv:2111.13823.

[59] H. Cheng, Q. Huang, H. He, Z. Zhao, H. Sun, Q. Wu, Z. Jiang, J. Wang, H. Huang, Z. Fu, and Y. Lu, Phys. Rev. Appl. **16**, 054011 (2021).

[60] P. Agarwal, L. Huang, S. Ter Lim, and R. Singh, Nat. Commun. **13**, 4072 (2022).

[61] L. Liu, C.-F. Pai, Y. Li, H. W. Tseng, D. C. Ralph, and R. A. Buhrman, Science **336**, 555 (2012).

[62] C.-F. Pai, L. Liu, Y. Li, H. W. Tseng, D. C. Ralph, and R. A. Buhrman, Appl. Phys. Lett. **101**, 122404 (2012).

[63] L. Liu, T. Moriyama, D. C. Ralph, and R. A. Buhrman, Phys. Rev. Lett. **106**, 036601 (2011).

[64] A. R. Mellnik, J. S. Lee, A. Richardella, J. L. Grab, P. J. Mintun, M. H. Fischer, A. Vaezi, A. Manchon, E.-A. Kim, N. Samarth, and D. C. Ralph, Nature (London) **511**, 499 (2014).

[65] M. DC, R. Grassi, J-Y. Chen, M. Jamali, D. R. Hickey, D. Zhang, Z. Zhao, H. Li, P. Quarterman, Y. Lv, M. Li, A. Manchon, K. A. Mkhoyan, T. Low, and J.-P. Wang, Nat. Mater. **17**, 800 (2018).

[66] N. H. D. Khang, Y. Ueda, and P. N. Hai, Nat. Mater. **17**, 808 (2018).

[67] See Supplemental Material at http://link.aps.org/supplemental/10.1103/PhysRevB.106.174401 for nonequilibrium (ultrafast demagnetization) and equilibrium (static) E-field sweep of the magnetic hysteresis loops.

[68] R. C. O'Handley, *Modern Magnetic Materials: Principles and Applications* (Wiley, New York, NY, 2000).

[69] L. Yuan, B. Wang, D. Zha, C. Liu, M. Li, Y. Xie, H. Yang, Y. Cao, H. Xu, and R.-W. Li, AIP Adv. **12**, 045203 (2022).

[70] P. V. Hendriksen, S. Linderoth, and P.-A. Lindgård, Phys. Rev. B **48**, 7259 (1993).

[71] G. Dos Santos, R. Aparicio, D. Linares, E. N. Miranda, J. Tranchida, G. M. Pastor, and E. M. Bringa, Phys. Rev. B **102**, 184426 (2020).

[72] S. Zhang, Q. Chen, Y. Liu, A. Chen, L. Yang, P. Li, S. Zhou, Y. Yu, W. Sun, X. Zhang, Y. Zhao, Y. Sun, and Y. Zhao, ACS Appl. Mater. Interfaces **9**, 20637 (2017).

[73] A. Chen, Y. Zhao, Y. Wen, L. Pan, P. Li, and X. Zhang, Sci. Adv. **5**, eaay5141 (2019).

[74] M. J. Jiménez, G. Cabeza, J. E. Gómez, D. Velázquez Rodriguez, L. Leiva, J. Milano, and A. Butera, J. Magn. Magn. Mater. **501**, 166361 (2020).

[75] N. N. Phuoc and C. K. Ong, J. Mater. Sci: Mater. Electron. **28**, 5628 (2017).

[76] Z. Zhou, S. Zhao, Y. Gao, X. Wang, T. Nan, N. X. Sun, X. Yang, and M. Liu, Sci. Rep. **6**, 20450 (2016).

[77] Y. Gao, X. Wang, L. Xie, Z. Hu, H. Lin, Z. Zhou, T. Nan, X. Yang, B. M. Howe, J. G. Jones, G. J. Brown, and N. X. Sun, Appl. Phys. Lett. **108**, 232903 (2016).

[78] Z. Hu, T. Nan, X. Wang, M. Staruch, Y. Gao, P. Finkel, and N. X. Sun, Appl. Phys. Lett. **106**, 022901 (2015).

[79] P. Koleják, G. Lezier, K. Postava, J.-F. Lampin, N. Tiercelin, and M. Vanwolleghem, ACS Photonics **9**, 1274 (2022).

[80] G. Lezier, P. Koleják, J.-F. Lampin, K. Postava, M. Vanwolleghem, and N. Tiercelin, Appl. Phys. Lett. **120**, 152404 (2022).

[81] F. Cheng, C. Wang, Z. Su, X. Wang, Z. Cai, N. X. Sun, and Y. Liu, Nano Lett. **20**, 6437 (2020).